MATHEMATICAL BIOSCIENCES
AND ENGINEERING
Volume **11**, Number **3**, June **2014**

doi:10.3934/mbe.2014.11.523

pp. **523–546**

EFFECT OF INTRAOCULAR PRESSURE ON THE HEMODYNAMICS OF THE CENTRAL RETINAL ARTERY: A MATHEMATICAL MODEL

Giovanna Guidoboni

Department of Mathematical Sciences
Indiana University - Purdue University at Indianapolis
Indianapolis, IN, USA
and
Department of Ophthalmology
Indiana University School of Medicine, Indianapolis, IN, USA

Alon Harris

Department of Ophthalmology
Department of Cellular & Integrative Physiology
Eugene and Marilyn Glick Eye Institute
Indiana University School of Medicine, Indianapolis, IN, USA

Lucia Carichino

Department of Mathematical Sciences
Indiana University - Purdue University at Indianapolis
Indianapolis, IN, USA

Yoel Arieli

Department of Electro Optics
Jerusalem College of Technology, Jerusalem, Israel

Brent A. Siesky

Department of Ophthalmology
Eugene and Marilyn Glick Eye Institute
Indiana University School of Medicine, Indianapolis, IN, USA

(Communicated by Mette Olufsen)

Abstract. Retinal hemodynamics plays a crucial role in the pathophysiology of several ocular diseases. There are clear evidences that the hemodynamics of the central retinal artery (CRA) is strongly affected by the level of intraocular pressure (IOP), which is the pressure inside the eye globe. However, the mechanisms through which this occurs are still elusive. The main goal of this paper is to develop a mathematical model that combines the mechanical action of IOP and the blood flow in the CRA to elucidate the mechanisms through which IOP elevation affects the CRA hemodynamics. Our model suggests that the development of radial compressive regions in the lamina cribrosa (a collagen structure in the optic nerve pierced by the CRA approximately in its center) might be responsible for the clinically-observed blood velocity reduction in the CRA following IOP elevation. The predictions of the mathematical model are

2010 *Mathematics Subject Classification.* Primary: 76Z05, 74F10, 74L15; Secondary: 76Z05.
Key words and phrases. Ocular blood flow, fluid-structure interaction, central retinal artery, intraocular pressure, lamina cribrosa.

in very good agreement with experimental and clinical data. Our model also identifies radius and thickness of the lamina cribrosa as major factors affecting the IOP-CRA relationship, suggesting that anatomical differences among individuals might lead to different hemodynamic responses to IOP elevation.

1. **Introduction.** Retinal hemodynamics plays a crucial role in the pathophysiology of several ocular diseases, including glaucoma, age-related macula degeneration and diabetic retinopathy [12, 14, 29, 31, 38, 39, 41, 47]. Even though clinical observations show significant correlations between alterations in retinal hemodynamics and vision impairment, the mechanisms giving rise to these correlations are not yet fully understood [6, 26, 30, 33]. The understanding of the mechanisms relating alterations in retinal hemodynamics and visual function could lead to significant improvement in the clinical management of patients and also aid the potential development of therapies targeting the modulation of ocular blood flow [6].

The retinal vascular bed nourishes the retinal ganglion cells that are responsible for the transmission of visual information from the retina to the brain, via the optic nerve. Blood is supplied by the *central retinal artery* (CRA), and drained by the central retinal vein, as shown in Figure 1(left). The figure shows that the central retinal vessels, i.e. central retinal artery and vein, run through the optic nerve canal, where they are exposed to the *retrolaminar tissue pressure* (RLTp), and they also enter inside the eye globe, where they are exposed to the *intraocular pressure* (IOP). The pressure difference between the RLTp in the optic nerve tissue (baseline value 7-10 mmHg) and the IOP inside the eye globe (baseline value 12-15 mmHg) is maintained by the *lamina cribrosa*, a collagen structure that is pierced by the central retinal vessels approximately in its center.

There are clear evidences that the CRA hemodynamics is strongly affected by the level of IOP inside the eye globe [27], but the mechanisms through which this occurs are still elusive. Mathematical modeling could help elucidating these mechanisms and, in addition, could help identifying the factors that influence the IOP-CRA relationship. To date though, mathematical models that combine the mechanical action of IOP and the blood flow in the retina are not available. Over the last two decades, diverse mathematical modeling techniques have been successfully utilized to understand and quantify the relationship between IOP elevation and the distributions of stress and strain in the optic nerve tissues, including the lamina cribrosa [5, 9, 11, 44, 45, 58, 55, 59, 60, 61]. In the recent years, few investigators have attempted the mathematical modeling of the retinal vasculature to assess the artero-venous distribution of hemodynamic parameters in the microvasculature[18, 19, 20, 21, 64], without accounting though for the vascular bio-mechanical response to IOP.

The main goal of this paper is to develop a mathematical model that combines, for the first time, the mechanical action of IOP and the blood flow in the retina. *In this paper we focus on the specific aim of elucidating the mechanisms through which IOP elevation affects the CRA hemodynamics.*

A schematic representation of the system described by our mathematical model is depicted in Figure 1(center). The lamina cribrosa is modeled as a nonlinear, homogeneous, isotropic, elastic circular plate of finite thickness, which deforms under the combined action of IOP, RLTp, and tension from the sclera (which is the outer shell of the eye), in the same spirit as, for example, [5, 9, 44, 45]. The CRA is modeled as a fluid-structure interaction system, where blood flow is modeled as the stationary Stokes flow of a Newtonian viscous fluid, while the arterial wall is

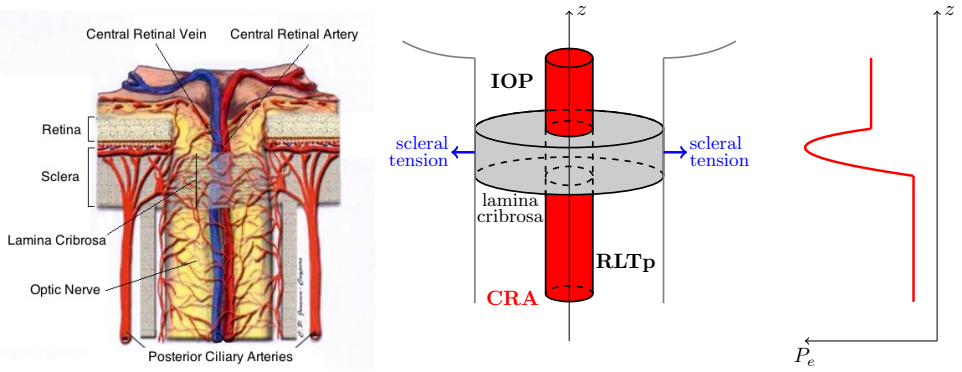

FIGURE 1. *Left: Anatomy of the central retinal vessels*, adapted from [28]. The central retinal artery (CRA) and vein run through the optic nerve canal where they are exposed to the retrolaminar tissue pressure (RLTp), and enter inside the eye globe where they are exposed to the intraocular pressure (IOP). The pressure difference between IOP and RLTp is mantained by the lamina cribrosa. The image shows the sclera, i.e. outer shell of the eye globe, which supports the retina and anchors the lamina cribrosa. The posterior ciliary arteries, shown in the picture, are not included in the mathematical model. *Center: Schematic representation of the mathematical model.* The main modeling components are the lamina cribrosa and the CRA running through it. *Right: External pressure acting on the CRA walls.* The CRA walls deform under the external pressure P_e which varies along the vessel length z to account for IOP, RLTp, and the presence of the lamina cribrosa.

modeled as a linear elastic cylindrical thick shell, in the same spirit as [40]. The walls of the CRA deform under the action of an external pressure P_e which varies along the vessel length z to account for the action of IOP, RLTp, and the presence of the lamina cribrosa, as shown in Figure 1(right). The values of the geometrical and material properties included in the model are taken from published literature, as summarized in Tables 1, 2 and 3. The predictions of the mathematical model are validated using three different and unrelated experimental and clinical studies. The experimental work by Morgan et al. [43] reports measurements of the IOP-induced displacement of the lamina cribrosa, while the clinical works by Harris et al. [27] and Findl et al. [13] report measurements of the IOP-induced decrease in CRA blood velocity.

The interpretation of the clinical data by Harris et al. and Findl et al. using our mathematical model suggest that the blood velocity reduction in the central retinal artery following IOP elevation is due to the development of regions of radial compressive stress in the lamina cribrosa, which constrict the central retinal artery running through it and consequently increase the CRA resistance to flow, inducing a reduction in blood flow velocity. Our model also suggests that variations in radius and thickness of the sclera and lamina cribrosa have a noticeable effect on the IOP-induced CRA hemodynamic alterations.

Several clinical and population-based studies have reported anatomical differences in ocular structures among individuals of different ethnicities [7, 8, 22, 23, 24, 25, 36, 48, 52, 54, 68], as well as racial differences in incidence and prevalence of ocular diseases, such as glaucoma [4, 32, 37, 51, 62, 63, 65, 66]. Our study shows that anatomical differences may induce significantly different hemodynamic responses in the central retinal artery for the same level of intraocular pressure. This might help explaining why certain individuals are more susceptible than others to ischemic damage in the optic nerve tissue even though they experience the same level of intraocular pressure, and might also help explaining why individuals of different ethnicity show different incidence and prevalence of ocular diseases.

The paper is organized as follows. The mathematical model is introduced in Section 2, its solution is described in Section 3. The results are presented in Section 4, and are discussed in Section 5. Conclusions are drawn in Section 6.

2. Mathematical model.

The model for the lamina cribrosa is described in Section 2.1, while the model for the central retinal artery is described in Section 2.2.

2.1. Lamina cribrosa.

The lamina cribrosa is modeled as a nonlinear, homogeneous, isotropic, elastic circular plate of radius R_{lc} and finite thickness h_{lc}, satisfying the equilibrium equations:

$$\nabla \cdot \mathbf{S} = \mathbf{0} \quad \text{in } \Omega \subset \mathbb{R}^3. \tag{1}$$

Here

$$\mathbf{S} = \lambda_{lc} \operatorname{tr}(\mathbf{E})\mathbf{I} + 2\mu_{lc}\mathbf{E} \quad \text{and} \quad \mathbf{E} = \frac{1}{2}[\nabla \mathbf{u} + (\nabla \mathbf{u})^T + (\nabla \mathbf{u})^T \nabla \mathbf{u}], \tag{2}$$

are the stress tensor and the Green-Saint-Venant strain tensor, $\mathbf{u}$ is the displacement vector, and λ_{lc} and μ_{lc} are the Lame's parameters that vary with the effective stress σ_e as reported in Table 1. The effective stress is defined as

$$\sigma_e = f(\mathbf{S}) = \sqrt{\frac{(S_{11} - S_{22})^2 + (S_{22} - S_{33})^2 + (S_{11} - S_{33})^2 + 6(S_{23}^2 + S_{31}^2 + S_{12}^2)}{2}}, \tag{3}$$

and the formula

$$\lambda_{lc} = \frac{\mu_{lc}(E_{lc} - 2\mu_{lc})}{3\mu_{lc} - E_{lc}}, \tag{4}$$

is used to relate λ_{lc}, the Young's modulus E_{lc}, and the shear modulus μ_{lc}. In

E_{lc} [MPa]	μ_{lc}[MPa]	Range of σ_e[MPa]
0.358	0.12	$0.008 > \sigma_e > 0.000$
0.656	0.22	$0.015 > \sigma_e > 0.008$
1.818	0.61	$\sigma_e > 0.015$

TABLE 1. Values of the Young's modulus E_{lc} and shear modulus μ_{lc} in the model for the lamina cribrosa as a function of the effective stress σ_e [45, 67].

cylindrical coordinates, the domain Ω can be written as

$$\Omega = \left\{ (s\cos\theta, s\sin\theta, \zeta) \in \mathbb{R}^3 \,:\, s \in [0, R_{lc}),\, \theta \in [0, 2\pi),\, \zeta \in \left(-\frac{h_{lc}}{2}, \frac{h_{lc}}{2}\right) \right\},$$

where s, θ and ζ denote the radial, azimuthal and axial Lagrangian coordinates, respectively. A sketch of the domain is drawn in Figure 2. We remark that our geometric representation of the lamina does not account for the central perforation which allows the passage of the CRA. However, Sigal et al. showed that this perforation has no significant effect on the stresses and strains in the lamina [55].

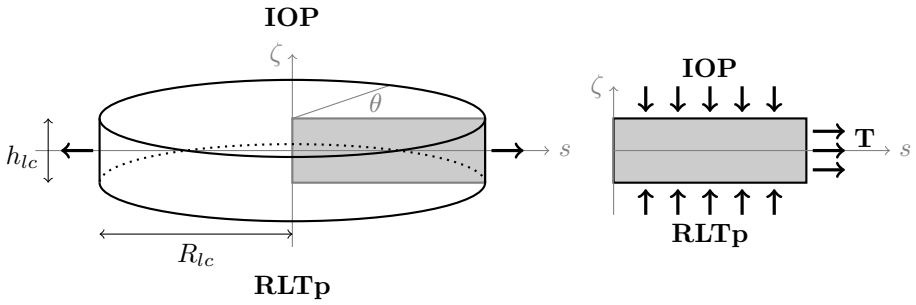

FIGURE 2. *Schematic representation of geometry and boundary conditions of the elasticity problem for the lamina cribrosa.* The anterior surface ($\zeta = h_{lc}/2$) is subject to the intraocular pressure (IOP), while the posterior surface ($\zeta = -h_{lc}/2$) is subject to the retrolaminar tissue pressure (RLTp). The lateral surface ($s = R_{lc}$) is connected to the sclera and experiences the scleral tension T.

The anterior circular surface of the lamina cribrosa faces the eye globe and is subject to the intraocular pressure, while the posterior circular surface faces the optic nerve canal and is subject to the retrolaminar tissue pressure. As a result, we impose the following boundary conditions:

$$\mathbf{S}\mathbf{n}_i = -\text{IOP}\,\mathbf{n}_i \quad \text{for } \zeta = \frac{h_{lc}}{2} \quad \text{and} \quad \mathbf{S}\mathbf{n}_o = -\text{RLTp}\,\mathbf{n}_o \quad \text{for } \zeta = -\frac{h_{lc}}{2}, \tag{5}$$

where $\mathbf{n}_i$ and $\mathbf{n}_o$ denote the outward normal vectors to the anterior and posterior surfaces. On its lateral surface, the lamina cribrosa is connected to the sclera and it experiences the scleral tension T, which results from the inflation due to the intraocular pressure. Following [9, 45], on the lateral surface we impose that

$$\mathbf{S}\mathbf{n}_l = T \quad \text{and} \quad u_\zeta = 0 \quad \text{for } s = R_{lc}, \tag{6}$$

where $\mathbf{n}_l$ is the outward normal vector to later surface, and T is computed using the Laplace's law

$$T = \frac{\text{IOP}\; R_s}{2h_s}, \tag{7}$$

where R_s and h_s are the scleral radius and thickness. We remark here that equation (7) comes with the assumption that the sclera can be modeled as a perfect sphere.

Taking advantage of the symmetry of geometry and boundary conditions, the problem can be simplified by assuming that its solutions are axially symmetric. This consists in assuming that the azimuthal displacement is equal to zero, i.e. $u_\theta = 0$, and that radial and axial displacements do not depend on the azimuthal angle θ, i.e. $u_s = u_s(s, \zeta)$ and $u_\zeta = u_\zeta(s, \zeta)$. Under these assumptions, the equilibrium

equations (1) reduce to

$$\begin{aligned} \frac{S_{ss}-S_{\theta\theta}}{s}+\frac{\partial S_{ss}}{\partial s}+\frac{\partial S_{s\zeta}}{\partial \zeta} &= 0, \\ \frac{S_{\zeta s}}{s}+\frac{\partial S_{\zeta s}}{\partial s}+\frac{\partial S_{\zeta\zeta}}{\partial \zeta} &= 0, \end{aligned} \tag{8}$$

defined on the rectangular domain $(0, R_{lc}) \times (-h_{lc}/2, h_{lc}/2)$ depicted in Figure 2 (right), with the boundary conditions

$$\begin{aligned} &S_{\zeta\zeta} = -\text{IOP}, \quad S_{s\zeta} = 0, && \text{for} \quad s \in (0, R_{lc}),\ \zeta = \frac{h_{lc}}{2}, \\ &S_{\zeta\zeta} = -\text{RLTp}, \quad S_{s\zeta} = 0, && \text{for} \quad s \in (0, R_{lc}),\ \zeta = -\frac{h_{lc}}{2}, \\ &S_{ss} = T, \quad u_\zeta = 0, && \text{for} \quad s = R_{lc},\ \zeta \in \left(-\frac{h_{lc}}{2}, \frac{h_{lc}}{2}\right), \\ &u_s = 0 \quad \text{and} \quad \frac{\partial u_\zeta}{\partial s} = 0 && \text{for} \quad s = 0. \end{aligned} \tag{9}$$

The components S_{ss}, $S_{\theta\theta}$, $S_{s\zeta}$, and $S_{\zeta\zeta}$ of the stress tensor can be written in terms of the components of the strain tensor E_{ss}, $E_{\theta\theta}$, $E_{s\zeta}$, and $E_{\zeta\zeta}$ as $S_{ss} = 2\mu_{lc}E_{ss}(\mathbf{u}) + \lambda_{lc}\,\mathrm{tr}\,\mathbf{E}(\mathbf{u})$, $S_{\theta\theta} = 2\mu_{lc}E_{\theta\theta}(\mathbf{u}) + \lambda_{lc}\,\mathrm{tr}\,\mathbf{E}(\mathbf{u})$, $S_{\zeta\zeta} = 2\mu_{lc}E_{\zeta\zeta}(\mathbf{u}) + \lambda_{lc}\,\mathrm{tr}\,\mathbf{E}(\mathbf{u})$, $S_{s\zeta} = 2\mu_{lc}E_{s\zeta}(\mathbf{u})$, where $\mathrm{tr}\,\mathbf{E}(\mathbf{u}) = E_{ss} + E_{\theta\theta} + E_{\zeta\zeta}$ and

$$\begin{aligned} E_{ss} &= \frac{\partial u_s}{\partial s} + \frac{1}{2}\left[\left(\frac{\partial u_s}{\partial s}\right)^2 + \left(\frac{\partial u_\zeta}{\partial s}\right)^2\right], \quad E_{\zeta\zeta} = \frac{\partial u_\zeta}{\partial \zeta} + \frac{1}{2}\left[\left(\frac{\partial u_s}{\partial \zeta}\right)^2 + \left(\frac{\partial u_\zeta}{\partial \zeta}\right)^2\right], \\ E_{\theta\theta} &= \frac{u_s}{s} + \frac{1}{2}\left(\frac{u_s}{s}\right)^2, \quad E_{s\zeta} = \frac{1}{2}\left[\frac{\partial u_s}{\partial \zeta} + \frac{\partial u_\zeta}{\partial s} + \frac{\partial u_s}{\partial s}\frac{\partial u_s}{\partial \zeta} + \frac{\partial u_\zeta}{\partial s}\frac{\partial u_\zeta}{\partial \zeta}\right]. \end{aligned} \tag{10}$$

2.2. **Central retinal artery.** The model for the compliant wall of the central retinal artery is described in Section 2.2.1, while the model for the blood flow inside the central retinal artery is described in Section 2.2.2.

2.2.1. *Central retinal artery: Arterial wall model.* The reference configuration of the arterial wall is a hollow circular cylinder of internal radius R_{cra} and thickness h_{cra}, see Figure 3, described by

$$\Omega^w_{cra} = \left\{(\eta\cos\phi, \eta\sin\phi, z) \in \mathbb{R}^3 \,:\, \eta \in (R_{cra}, R_{cra}+h_{cra}),\ \phi \in [0, 2\pi),\ z \in (0, L)\right\},$$

where (η, ϕ, z) are the radial, azimuthal, and axial lagrangian coordinates, respectively. The superscript w indicates that the domain Ω^w_{cra} represents the wall of the central retinal artery. Under the assumptions that:

1. the deformation of the arterial wall obeys the linear theory of elasticity;
2. the axial displacement is negligible with respect to the radial displacement;
3. geometry, loading and solutions are axially symmetric;

the equilibrium equation for the arterial wall reduces to

$$\frac{\partial}{\partial \eta}\left[\frac{1}{\eta}\frac{\partial}{\partial \eta}(\eta u_\eta)\right] = 0 \quad \text{for} \quad (\eta, z) \in (R_{cra}, R_{cra}+h_{cra}) \times (0, L), \tag{11}$$

where $u_\eta = u_\eta(\eta, z)$ denotes the radial displacement. Equation (11) necessitates boundary conditions for the external and internal cylindrical surfaces located at $\eta = R_{cra} + h_{cra}$ and $\eta = R_{cra}$, respectively.

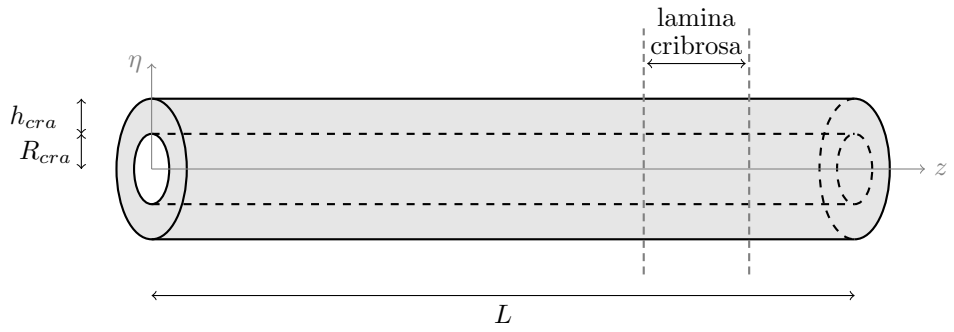

FIGURE 3. *Representation of the wall of the central retinal artery (CRA).* The reference configuration of the CRA wall is a hollow circular cylinder of internal radius R_{cra} and thickness h_{cra}. The vertical dashed lines indicate the location of the lamina cribrosa with respect to the CRA axis.

On the external surface located at $\eta = R_{cra} + h_{cra}$, we prescribe the normal stress through the condition

$$\left[\lambda_{cra}\frac{u_\eta}{\eta} + (2\mu_{cra} + \lambda_{cra})\frac{\partial u_\eta}{\partial \eta}\right]_{\eta=R_{cra}+h_{cra}} = -P_e(z), \tag{12}$$

where λ_{cra} and μ_{cra} are the Lame's constants which are related to the Young's modulus E_{cra} and the Poisson's ratio ν_{cra} by

$$\lambda_{cra} = \frac{E_{cra}\nu_{cra}}{(1+\nu_{cra})(1-2\nu_{cra})} \quad \text{and} \quad \mu_{cra} = \frac{E_{cra}}{2(1+\nu_{cra})}. \tag{13}$$

The external pressure $P_e(z)$ varies along the length of the vessel, accounting for the action of the intraocular pressure, retrolaminar tissue pressure, and the presence the lamina cribrosa. More precisely, we write $P_e(z)$ as

$$P_e(z) = \begin{cases} \text{RLTp} & \text{for} \quad 0 \le z < z_{lc,c}, \\ -S_{ss}(0, t(z)) & \text{for} \quad z_{lc,c} \le z \le z_{lc}, \\ \text{IOP} & \text{for} \quad z_{lc} < z < L, \end{cases} \tag{14}$$

where S_{ss} represents the compression exerted by the lamina cribrosa on the wall of the central retinal artery, the coordinate $z = z_{lc}$ indicates the relative position of the anterior surface of the lamina cribrosa with respect to the CRA axis, while the coordinate $z = z_{lc,c}$ indicates the lower end of the compressive region in the lamina, as shown in Figure 4. More precisely, we define $z_{lc,c}$ as

$$z_{lc,c} = \min\{z \in (z_{lc} - h_{lc}, z_{lc}) \,:\, -S_{ss}(0, t(z)) \ge \text{RLTp}\}, \tag{15}$$

where $t(z) = z - z_{lc} + h_{lc}/2$.

Remark 1. The radial stress along the central axis of the lamina cribrosa is given by S_{ss} evaluated at $s = 0$. Radial compressive stress corresponds to negative values of S_{ss}, and it translates into a positive contribution to the external pressure P_e acting on the CRA wall via equation (14).

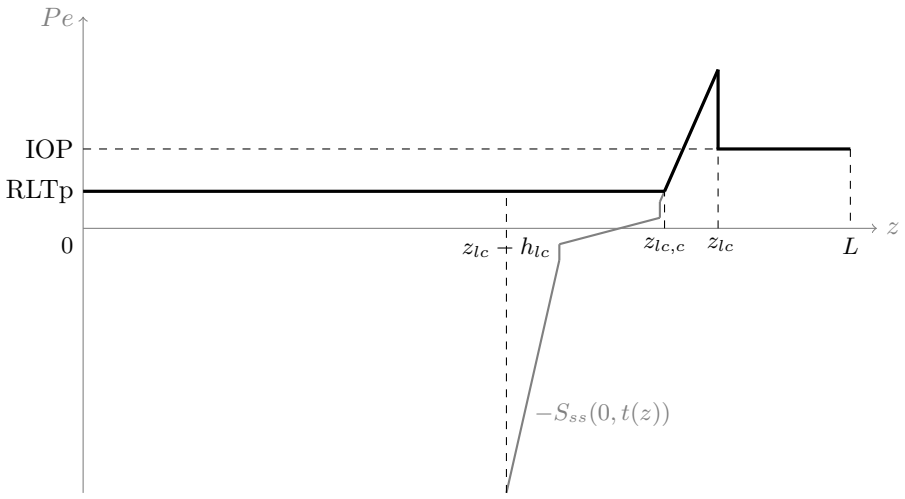

FIGURE 4. *Representation of the external pressure P_e acting on the wall of the central retinal artery.* P_e varies along the length z of the central retinal artery, accounting for the intraocular pressure IOP, retrolaminar tissue pressure RLTp, and the compression from the lamina cribrosa $S_{ss}(0, t(z))$.

On the internal surface located at $\eta = R_{cra}$ representing the interface between arterial wall and blood, we impose the balance of stress

$$\left[\lambda_{cra}\frac{u_\eta}{\eta} + (2\mu_{cra} + \lambda_{cra})\frac{\partial u_\eta}{\partial \eta}\right]_{\eta=R_{cra}} = -\Psi(z), \tag{16}$$

where $\Psi(z)$ is the function describing the action of blood flow on the arterial wall and will be defined later (see equation (22)).

2.2.2. *Central retinal artery: Blood flow model.* The domain Ω^b_{cra} occupied by the blood inside the central retinal artery is represented in Figure 5 and is defined as

$$\Omega^b_{cra} = \left\{(r\cos\phi, r\sin\phi, z) \in \mathbb{R}^3 \,:\, r \in [0, \gamma(z)),\ \phi \in [0, 2\pi),\ z \in (0, L)\right\},$$

where (r, ϕ, z) are the radial, azimuthal, and axial eulerian coordinates, respectively. Here $\gamma(z)$ describes the wall/blood interface in eulerian coordinates and it is related to the radial displacement of the wall by

$$\gamma(z) = R_{cra} + u_\eta(R_{cra}, z). \tag{17}$$

We remark here that we are using the same azimuthal and axial coordinates ϕ and z for both the lagrangian and eulerian frameworks. This is not justifiable in general, but in our case it is justified by the assumptions of axial symmetry and negligibility of the arterial wall displacement in the axial direction. Under the assumptions that:

1. the blood can be described as a Newtonian incompressible viscous fluid;
2. the pressure depends only on z;
3. the radial velocity is negligible in the balance of axial momentum;
4. geometry, loading and solutions are axially symmetric;

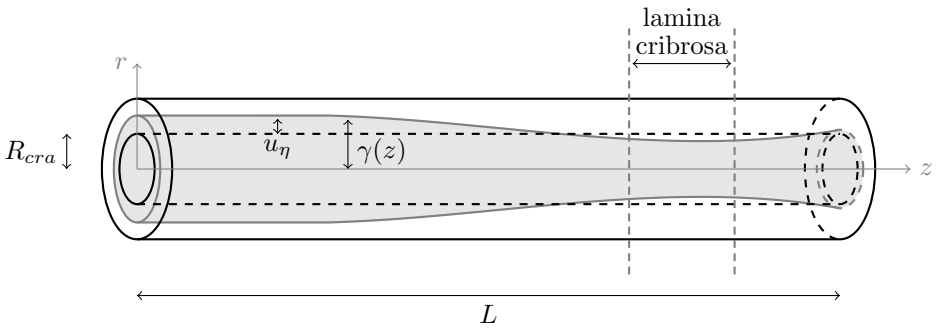

FIGURE 5. *Domain occupied by the blood flowing inside the central retinal artery (CRA).* The function $\gamma(z)$ describes the wall/blood interface in eulerian coordinates, R_{cra} is the reference radius of the CRA, and u_η is the radial displacement of the arterial wall. The vertical dashed lines indicate the location of the lamina cribrosa with respect to the CRA axis.

the equations of conservation of mass and balance of axial momentum describing blood flow in the central retinal artery reduce to

$$\frac{1}{r}\frac{\partial}{\partial r}(rv_r) + \frac{\partial v_z}{\partial z} = 0, \tag{18}$$

$$\mu_b \frac{1}{r}\frac{\partial}{\partial r}\left(r\frac{\partial v_z}{\partial r}\right) = \frac{dp}{dz}, \tag{19}$$

for $(r,z) \in [0,\gamma(z)) \times (0,L)$, where $v_r = v_r(r,z)$ and $v_z = v_z(r,z)$ denote the radial and axial components of the blood velocity, respectively, $p = p(z)$ denotes the pressure, and μ_b denotes the blood (effective) viscosity. We remark that the assumption of Newtonian fluid is justified by [49], where a nearly parabolic profile is reported for the blood velocity in retinal arteries of diameter larger than 100μm.

System (18)-(19) must be completed with boundary conditions in both radial and axial directions. At the inlet and outlet sections of the vessel, we prescribe

$$p = P_0 \quad \text{for } z = 0, \quad \text{and} \quad p = P_L \quad \text{for } z = L, \tag{20}$$

where P_0 and P_L are assumed to be known values. At the blood/arterial wall interface, we impose the no-slip condition

$$v_r = 0 \quad \text{and} \quad v_z = 0 \quad \text{for} \quad r = \gamma(z), \tag{21}$$

and the balance of stress condition (16), where the function $\Psi(z)$ is given by

$$\Psi(z) = \frac{\gamma(z)p(z)}{R_{cra}}, \tag{22}$$

if we assume that the effect of shear stress is negligible in comparison to pressure. It is worth noticing that the function Ψ does not simply equal p, but it involves the product between p and γ. This is due to the nonlinear coupling between lagrangian and eulerian coordinates at the wall/blood interface.

3. **Solution procedure.** The model described in Section 2 is solved in three steps:

   Step 1: solve system (8)-(9) to calculate the stress in the lamina cribrosa;
   Step 2: determine P_e in (14), given the stress from Step 1;
   Step 3: solve system (11)-(22) to calculate blood velocity, blood pressure, and wall/blood interface (lumen) of the central retinal artery.

Details about Step 1 and Step 3 and given in the subsections below.

3.1. **Step 1.** System (8)-(9) includes:

- *material nonlinearities*: the Lame's properties are not given a priori but they depend on the solution itself via the effective stress, as shown in equation (3) and Table 1;
- *geometric nonlinearities*: the Green-Saint Venant strain tensor includes quadratic terms in the derivatives of the displacement to account for large deformations, as shown in equation (2).

To address these nonlinearities, we designed the iterative algorithm described below.

Let σ_e^0 (and therefore λ_{lc}^0 and μ_{lc}^0) be given. For $n \geq 1$ proceed as follows:

1. compute $\mathbf{u}^n$ via the fixed point iterations:
   let $\mathbf{w}^0$ be given (equal to $\mathbf{u}^{n-1}$ if $n > 1$, equal to $\mathbf{0}$ otherwise), for $j \geq 1$:

   (a) compute $\mathbf{w}^j$ as the solution of the variational problem

$$
\begin{aligned}
&2\int_0^{R_{lc}} \int_{-\frac{h_{lc}}{2}}^{\frac{h_{lc}}{2}} \mu_{lc}^n \, \mathbf{E}\left(\mathbf{w}^j, \mathbf{w}^{j-1}\right) : \mathbf{L}(\mathbf{v}) \; s \, ds \, d\zeta + \\
&+ \int_0^{R_{lc}} \int_{-\frac{h_{lc}}{2}}^{\frac{h_{lc}}{2}} \lambda_{lc}^n \left(\operatorname{tr} \mathbf{E}\left(\mathbf{w}^j, \mathbf{w}^{j-1}\right)\right) \left(\mathbf{I} : \mathbf{L}(\mathbf{v})\right) \; s \, ds \, d\zeta = \\
&- \int_0^{R_{lc}} \mathrm{IOP} \, v_\zeta \Big|_{\zeta = h_{lc}/2} s \, ds + \int_0^{R_{lc}} \mathrm{RLTp} \, v_\zeta \Big|_{\zeta = -h_{lc}/2} s \, ds + \\
&+ \int_{-\frac{h_{lc}}{2}}^{\frac{h_{lc}}{2}} R_{lc} \, T \, v_s \Big|_{s = R_{lc}} d\zeta \qquad \forall \mathbf{v} = (v_s, v_\zeta) \in V,
\end{aligned}
\tag{23}
$$

   where $V = \left\{ \mathbf{v} \in \left(H^1(C)\right)^2 \, : \, v_\zeta \Big|_{s=R_{lc}} = 0, \; v_s \Big|_{s=0} = 0 \right\}$,

   with $\mathbf{L}(\mathbf{v}) = \left[\nabla \mathbf{v} + (\nabla \mathbf{v})^T\right]/2$, $\mathbf{E}\left(\mathbf{w}^j, \mathbf{w}^{j-1}\right) = \mathbf{L}(\mathbf{w}^j) + \mathbf{N}\left(\mathbf{w}^j, \mathbf{w}^{j-1}\right)$, $\mathbf{N}(\mathbf{q}, \mathbf{t}) = \left[(\nabla \mathbf{q})^T \nabla \mathbf{t} + (\nabla \mathbf{t})^T \nabla \mathbf{q}\right]/4$, and $C = (0, R_{lc}) \times (-h_{lc}/2, h_{lc}/2)$.

   (b) test for convergence:
   if $\dfrac{\|\mathbf{w}^j - \mathbf{w}^{j-1}\|_{L^2(\Omega)}}{\|\mathbf{w}^j\|_{L^2(\Omega)}} < \varepsilon_1$ set $\mathbf{u}^n = \mathbf{w}^j$ and go to point 2,
   otherwise set $\mathbf{w}^{j-1} = \mathbf{w}^j$ and go back to point (a).

2. compute $\mathbf{S}^n = 2\mu_{lc}^n \, \mathbf{E}(\mathbf{u}^n) + \lambda_{lc}^n \, \mathrm{tr}\mathbf{E}(\mathbf{u}^n)\mathbf{I}$;
3. compute $\sigma_e^n = f(\mathbf{S}^n)$ (3);

4. test for convergence:
   if $\|\sigma_e^n - \sigma_e^{n-1}\|_{L^\infty(\Omega)} < \varepsilon_2$ go to point 5
   otherwise set $\sigma_e^{n-1} = \sigma_e^n$, update λ_{lc}^n and μ_{lc}^n and go back to point 1.

5. set the solution of the system to be $\mathbf{u} = \mathbf{u}^n$ and $\mathbf{S} = \mathbf{S}^n$.

This algorithm has been implemented in FreeFem++, a Finite Element Method-based software for the solution of PDEs [15], using quadratic finite elements on a regular and uniform 50×100 triangulation, with $\varepsilon_1 = \varepsilon_2 = 10^{-5}$.

3.2. **Step 3.** System (11)-(22) can be solved analytically. The radial displacement of the arterial wall is computed as the solution of equation (11) with the boundary conditions (12) and (16), leading to

$$u_\eta(\eta, z) = \Big(a_1\gamma(z)p(z) - a_2P_e(z)\Big)\eta + \left(\frac{\gamma(z)p(z)}{R_{cra}} - P_e(z)\right)\frac{a_3}{\eta}, \tag{24}$$

where

$$\begin{aligned} a_1 &= \frac{1}{2(\lambda_{cra}+\mu_{cra})}\frac{R_{cra}}{h_{cra}(h_{cra}+2R_{cra})}, \\ a_2 &= a_1\frac{(h_{cra}+R_{cra})^2}{R_{cra}}, \\ a_3 &= a_2\left(1+\frac{\lambda_{cra}}{\mu_{cra}}\right)R_{cra}(h_{cra}+R_{cra})^2. \end{aligned} \tag{25}$$

Using now the geometric relation (17), we obtain

$$\begin{aligned} \gamma(z) &= R_{cra} + u_\eta(R_{cra}, z) \\ &= \Big(1 + a_1\gamma(z)p(z) - a_2P_e(z)\Big)R_{cra} + \left(\frac{\gamma(z)p(z)}{R_{cra}} - P_e(z)\right)\frac{a_3}{R_{cra}}. \end{aligned} \tag{26}$$

Solving (26) for $\gamma(z)$ we obtain

$$\gamma(z) = R_{cra}\,\frac{1 - b_1P_e(z)}{1 - b_2p(z)}, \tag{27}$$

where

$$b_1 = a_2 + \frac{a_3}{R_{cra}^2} \quad \text{and} \quad b_2 = a_1R_{cra} + \frac{a_3}{R_{cra}^2}. \tag{28}$$

Let us now consider the equations describing blood flow. By integrating equation (19) with respect to r, we obtain that

$$v_z(r, z) = \frac{1}{4\mu_b}\left[r^2 - (\gamma(z))^2\right]\frac{dp}{dz}. \tag{29}$$

By integrating equation (18) with respect to r, using (21) and (29), we obtain

$$\frac{d}{dz}\left[(\gamma(z))^4\frac{dp}{dz}(z)\right] = 0. \tag{30}$$

Now equations (27) and (30) form a system in the unknowns $\gamma(z)$ and $p(z)$ that can be solved to obtain

$$p(z) = \frac{1}{b_2}\left[1 - \left(C_0\int_0^z (1 - b_1P_e(t))^{-4}dt + C_1\right)^{-1/3}\right], \tag{31}$$

and

$$\gamma(z) = R_{cra}\Big(1 - b_1P_e(z)\Big)\left(C_0\int_0^z (1 - b_1P_e(t))^{-4}dt + C_1\right)^{1/3}, \tag{32}$$

where $P_e(z)$ is given by (14), while the integration constants C_0 and C_1 are obtained using the boundary conditions (20) and are given by

$$C_0 = \frac{(1-b_2P_L)^{-3} - (1-b_2P_0)^{-3}}{\int_0^L (1-b_1P_e(t))^{-4}dt} \quad \text{and} \quad C_1 = (1-b_2P_0)^{-3}. \tag{33}$$

The solution of system (31)-(33) has been implemented in MATLAB, a numerical computing environment.

4. **Results.** The displacement of the lamina cribrosa predicted by our mathematical model for different values of IOP and retrolaminar tissue pressure has been compared with the experimental data obtained by Morgan et al [43]. Here, the anterior chamber and lateral ventricles of the eyes of eight mixed-breed dog were cannulated to sequentially increase IOP and cerebrospinal fluid pressure (CSFp). Confocal scanning laser tomography was performed at each level of IOP and CSFp to measure the depth of the optic disc surface, which reflects the underlying anterior laminar movement. Starting from baseline (corresponding to IOP= 15 mmHg and CSFp= 0 mmHg), IOP was elevated up to an average of 32 mmHg, via steps between 3 and 5 mmHg. A second set of experiments were performed in which, starting from baseline, CSFp was elevated up to an average of 12 mmHg, via steps between 2 and 4 mmHg. Morgan et al. report their results using the quantity ΔMaxD, which represents the difference in the maximum disc depth with respect to baseline. Experimental data are shown in Figure 6.

In order to compare the predictions of our mathematical model with the experimental data, we used the following linear relation between CSFp and RLTp (in mmHg), derived by Morgan et al. in a previous work [42]:

$$\text{RLTp} = \begin{cases} 0.07\,\text{CSFp} + 2.9200 & \text{for} \quad \text{CSFp} \leq 1.33, \\ 0.82\,\text{CSFp} + 1.9225 & \text{for} \quad \text{CSFp} > 1.33. \end{cases} \tag{34}$$

Then, we solved the system (8)-(9) with RLTp= 2.92 mmHg, which corresponds to CSFp= 0 mmHg via (34), and with IOP varying between 15 mmHg and 32.5 mmHg. Next, we solved the system (8)-(9) with IOP= 15 mmHg, and with RLTp varying in the range that corresponds to CSFp between 0 mmHg and 12 mmHg via (34). Since geometric and elastic properties of the eyes examined in [43] are not reported in the article, we chose physiologically representative values as by published literature, see Tables 1 and 2.

Parameter	Values	Unit	Source
R_{lc}	0.75	[mm]	[34]
h_{lc}	0.2	[mm]	[35, 53]
R_s	12	[mm]	[35, 46]
h_s	1	[mm]	[46, 53]

TABLE 2. Values of the parameters in the model for the lamina cribrosa.

The maximum disc depth ΔMaxD measured by Morgan et al. is compared with the anterior laminar displacement computed via our mathematical model, namely

u_ζ at $s = 0$ and $\zeta = h_{lc}/2$. The comparison between model predictions and experimental data is reported in Figure 6.

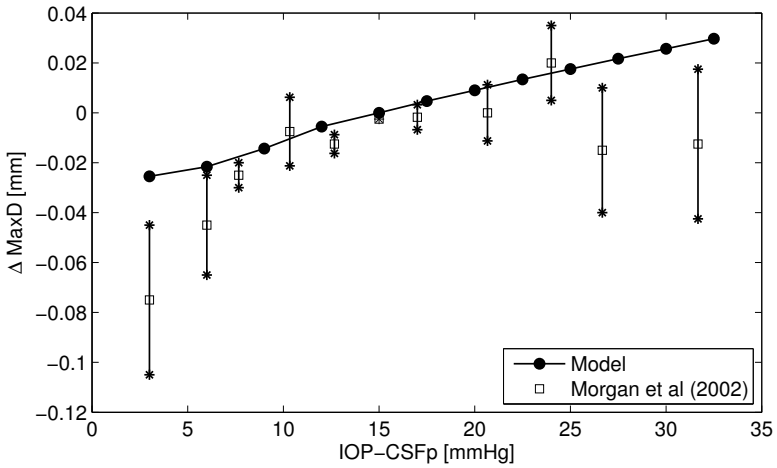

FIGURE 6. *Comparison between model predictions and experimental measurements of the anterior lamina displacement.* Increments of maximum disc depth ΔMaxD with respect to the baseline IOP-CSFp= 15 mmHg are reported as a function of the IOP-CSFp difference. The predictions of the mathematical model (*solid line*) are compared with experimental data by Morgan et al. [43].

The mathematical model is also used to calculate the radial stress component S_{ss} arising in the lamina cribosa for different IOP values. The results are reported in Figure 7 and they show regions of radial compressive stress in the lamina cribrosa, corresponding to negative values of S_{ss}. These regions become more pronounced as IOP is elevated.

The value of S_{ss} along the central axis of the lamina is of particular interest here, since it affects the pressure acting on the external wall of the central retinal artery via (14). Figure 8 shows the behavior of S_{ss} for $s = 0$ as a function of the axial coordinate ζ across the lamina's thickness, for different IOP values. The significance of compressive regions, corresponding to negative values of S_{ss}, increases with IOP both in terms of magnitude and depth penetration in the lamina's thickness.

IOP elevation also induces an increases in scleral tension, as dictated by the Laplace's law (7). This increase in scleral tension contributes to relieve some (but not all) of the radial compression in the lamina cribrosa, as shown in Figure 9. The solid lines correspond to the case where the scleral tension varies with IOP according to the Laplace's law, while the dashed lines corresponds to the case where the scleral tension is held constant at its value for IOP = 20 mmHg.

The IOP-induced reduction in the CRA blood velocity predicted by our mathematical model has been compared to the clinical data reported by two independent studies, namely Harris et al [27] and Findl et al [13]. Since the studies do not report geometrical and material properties of the central retinal artery, we have

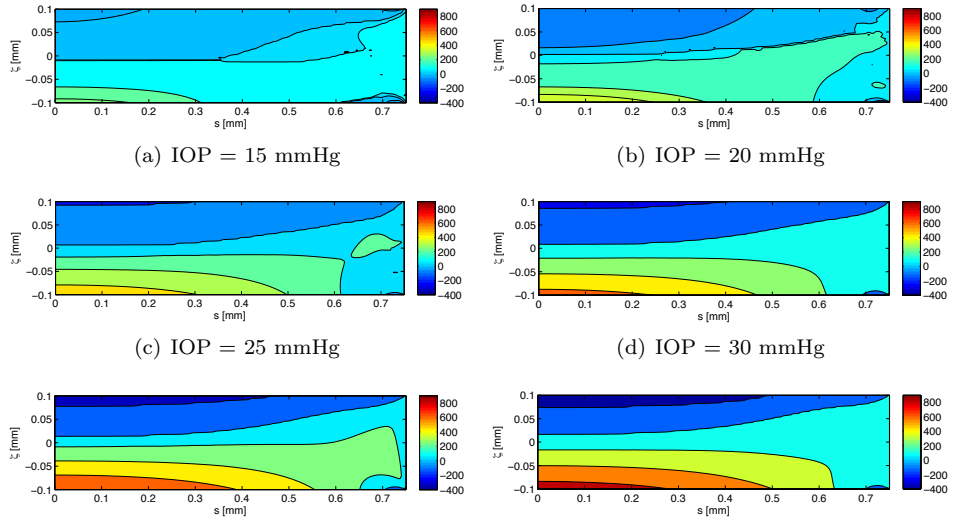

(a) IOP = 15 mmHg (b) IOP = 20 mmHg

(c) IOP = 25 mmHg (d) IOP = 30 mmHg

(e) IOP = 35 mmHg (f) IOP = 40 mmHg

FIGURE 7. *Radial stress* S_{ss} [mmHg]. Distribution of the radial stress in the lamina cribrosa for different IOP values. Regions of radial compressive stress correspond to negative values of S_{ss}.

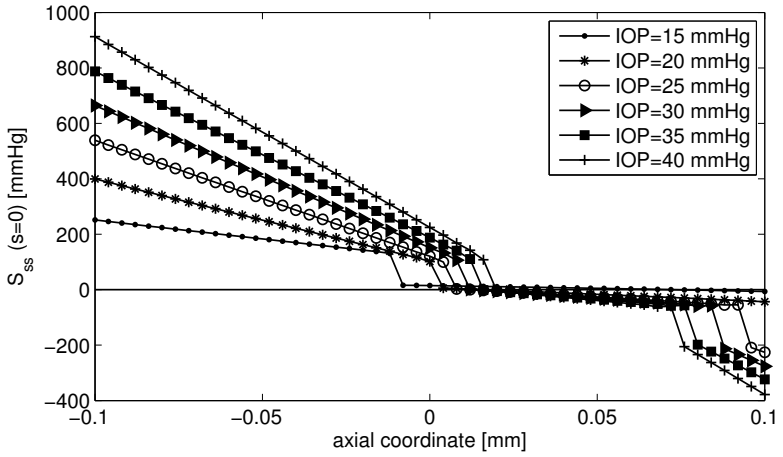

FIGURE 8. *Effect of IOP elevation on the radial stress* S_{ss}. The radial stress S_{ss} along the central axis of the lamina ($s = 0$) is reported as a function of the axial coordinate ζ across the lamina's thickness, for different IOP values.

used physiologically representative values as by published literature, summarized in Table 3.

Remark 2. The length of the whole CRA is approximately 10-15 mm, but we chose $L = 1.5$ mm since we are considering only a small segment of the CRA around the

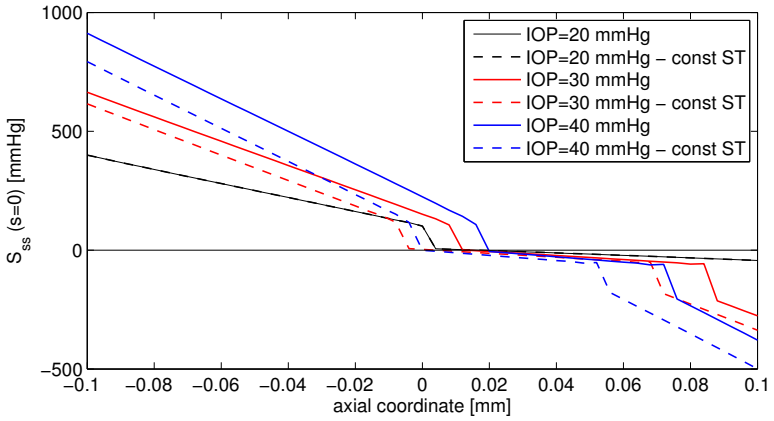

FIGURE 9. *Effect of the scleral tension on the radial stress* S_{ss}. The radial stress S_{ss} along the central axis of the lamina ($s = 0$) is reported as a function of the axial coordinate ζ across the lamina's thickness, for different IOP values and with the scleral tension increasing with IOP via the Laplace's law (*solid lines*) or with scleral tension held constant at its value for IOP=20 mmHg (*dashed lines*).

site of interest, namely the region of the optic nerve head where the CRA runs through the lamina cribrosa.

Remark 3. The pressure P_L at the outlet section of the CRA was chosen following [64], while the inlet pressure P_0 was estimated using the Poiseuille's law

$$P_0 = P_L + \frac{4\mu_b L V}{R_{cra}^2}, \tag{35}$$

where the characteristic velocity V at the vessel centerline is chosen as $V = 6.25$ cm/s to be consistent with the values measured by Harris et al. [27] and Findl et al. [13].

Parameter	Values	Unit	Source
R_{cra}	75	[μm]	[10]
h_{cra}	20	[μm]	[3]
L	1.5	[mm]	
z_{lc}	$L - 0.75$	[mm]	
E_{cra}	0.3	[MPa]	[2, 17, 50]
ν_{cra}	0.49	[1]	[2, 17, 50]
μ_b	0.003	[Pa s]	[16, 50]
P_L	39.5	[mmHg]	[64]

TABLE 3. Values of the parameters in the model for the CRA.

In the study by Harris et al., the IOP was artificially elevated on eleven healthy individuals using suction opthalmodynamometry, from a baseline near 14 mmHg to approximately 45 mmHg in 3-4 increments. At each IOP level, peak systolic and end diastolic velocities (PSV and EDV) were measured in the central retinal artery using Color Doppler Imaging. The measurements were performed at an intermediate location between the lamina cribrosa and the eye globe, corresponding to $z = L$ in our model. Thus, we solved systems (8)-(9) and (24)-(33) setting RLTp = 7 mmHg, and varying IOP between 15 and 40 mmHg. Figure 10 shows the comparison between the centerline velocity at the outlet section of the CRA measured by Harris et al. [27] and predicted by our mathematical model. Even though our stationary model provides only a mean value of the velocity, the model predictions fall nicely in the band between the values of peak systolic and end diastolic velocities measured in vivo.

In order to assess whether or not the radial compressive stress in the lamina cribrosa is contributing to the observed decrease in CRA blood velocity, we have run simulations where the radial compressive stress has been taken into account, meaning P_e defined as in (14) (solid blue curve), and where the radial compressive stress has not been taken into account, meaning P_e = RLTp up to z_{lc} (solid red curve). In both cases though, the IOP is acting directly on the post-laminar segment of the CRA, since P_e = IOP for $z > z_{lc}$. The model predictions obtained by taking into account the lamina compression show a similar behavior as the in vivo measurements, with a noticeable decrease in velocity as IOP increases from 15 to 40 mmHg. In the study by Findl et al., the CRA blood flow velocity was measured by

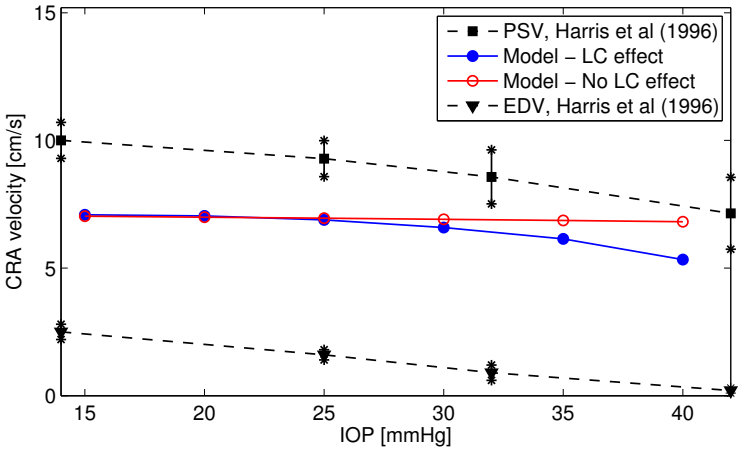

FIGURE 10. *Effect of IOP elevation on the peak systolic velocity (PSV) and end diastolic velocity (EDV) of the blood flow in the CRA.* Comparison between in vivo measurements by Harris et al. [27] (*black*) and model predictions obtained by taking (*blue*) or not taking (*red*) into account the lamina compression on the CRA.

Doppler sonography on 10 healthy individuals, while IOP was elevated artificially using a suction cup. In each subject, the IOP was increased of 10 mmHg and of 20 mmHg with respect to its baseline value, and the mean velocity of the CRA

blood flow was measured at approximately 3 mm behind the optic disc surface, corresponding to $z = 0$ in our model. This study reported a decrease in the CRA blood flow velocity following IOP elevation. The decrease was $-5 \pm 3\%$ at $+10$ mmHg and $-14 \pm 5\%$ at $+20$ mmHg ($p < 0.005$). In order to compare the predictions of our mathematical model with the data by Findl et al., we solve the system (8)-(9) and (24)-(33) setting RLTp = 7 mmHg, and for IOP equal to 11.3 mmHg (mean value of the baseline IOP in Findl et al), 21.3 mmHg and 31.3 mmHg, with and without taking into account the compression effect from the lamina cribrosa. Figure 11 shows the comparison between the percent change of the centerline velocity at the inlet section of the CRA, i.e. $v_z(r = 0, z = 0)$, predicted by our mathematical model (blue and red histograms) and measured in vivo by Findl et al. (gray histograms). If the lamina compression is included, our model predicts a decrease of -4.54% at $+10$ mmHg and -14.79% at $+20$ mmHg, showing a very good agreement with the clinical data. If the lamina compression is not included, our model predicts a decrease of -4.68% at $+10$ mmHg and -9.34% at $+20$ mmHg.

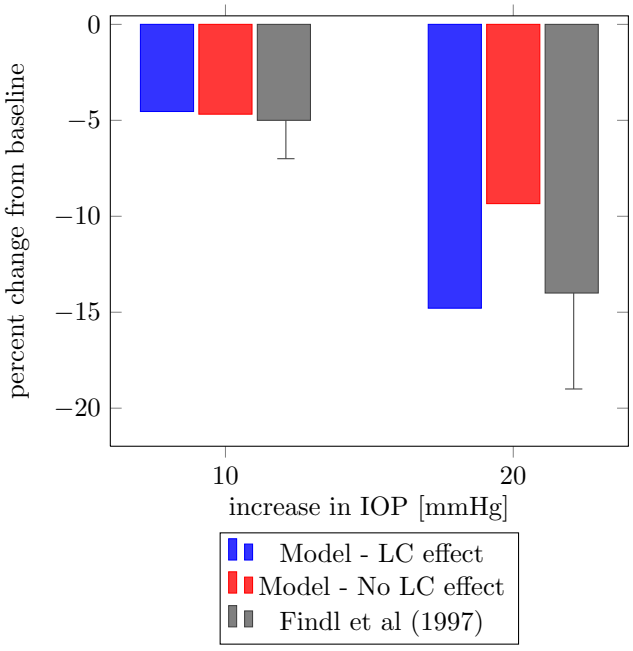

FIGURE 11. *Comparison of percent decrease in the mean CRA centerline velocity with IOP elevation.* Comparison between in vivo measurements by Findl e al. [13] (*gray*) and model predictions obtained by taking (*blue*) or not taking (*red*) into account the lamina compression on the CRA.

Our model also predicts that the decrease in centerline velocity at the outlet section of the CRA segment combines with a decrease in the lumen, resulting in a decrease of the flow rate Q^* defined as

$$Q^* = \int_0^{2\pi} \int_0^{\gamma^*} v_z(r, L) r dr \, d\theta, \tag{36}$$

with $\gamma^* = \gamma(z = L)$, and of the resistance $R = (P_L - P_0)/Q^*$, as IOP increases from 15 to 40 mmHg. The results are shown in Figure 12.

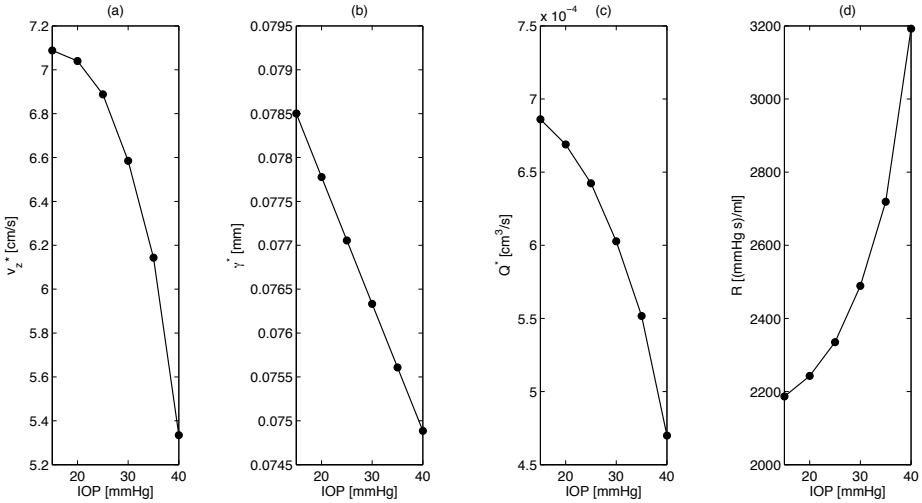

FIGURE 12. *Effect of IOP elevation on CRA hemodynamics.* Centerline velocity (a), CRA lumen (b), flow rate (c) and resistance (d) at the outlet section of the CRA ($z = L$) as a function of IOP, as predicted by our mathematical model.

Figure 13 shows the comparison between the decreases in the centerline velocity v_z^* and in the flow rate Q^* induced by IOP elevation, after normalization with respect to their values at IOP = 15 mmHg, as predicted by our mathematical model. The results show that the decrease in flow rate with IOP elevation is even more pronounced than the decrease in velocity detectable with the Color Doppler Imaging in vivo. This information might be useful in interpreting clinical measurements.

We have also used the model to investigate the effect of variations in scleral radius R_s, scleral thickness h_s, laminar radius R_{lc} and laminar thickness h_{lc} on the flow rate Q^* in the CRA. More precisely, we have considered baselines values of $R_s = 12$ mm, $h_s = 1$ mm, $R_{lc} = 0.75$ mm and $h_{lc} = 0.2$ mm, and we have varied one parameter at a time for different IOP values. Results are presented in Figure 14, where h_{lc} varies between 0.18 and 0.22 mm [35, 53], R_{lc} between 0.65 and 0.85 mm [34, 46], h_s between 0.8 and 1.2 mm [46, 53], R_s between 10 and 14 mm[46, 35], IOP equal to 20, 30, and 40 mmHg and RLTp equal to 7 mmHg. The results show that the flow rate of Q^* increases as h_{lc} and R_s increase, while Q^* decreases as R_{lc} and h_s increase. It is interesting to notice that the values of Q^* are particularly sensitive to geometrical variations of the lamina cribrosa.

5. **Discussion.** The results presented in the previous section suggest that the clinically-observed blood velocity reduction in the central retinal artery following IOP elevation maybe due to the following mechanism:

- IOP elevation induces a larger pressure difference across the lamina cribrosa;
- a region of radial compressive stress arises in the lamina cribrosa constricting the central retinal artery running through it;

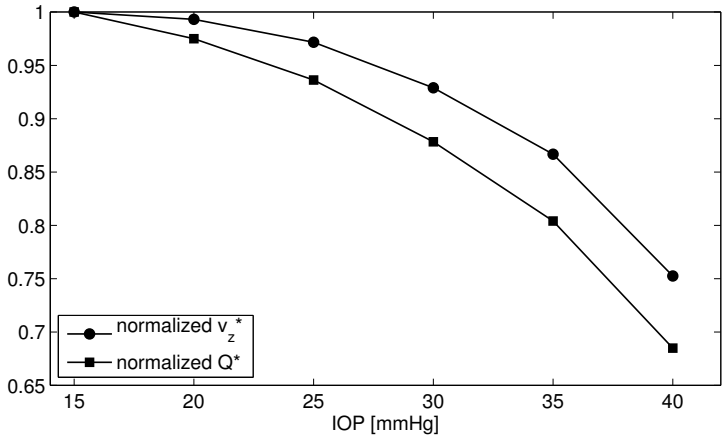

FIGURE 13. *Effect of IOP elevation on normalized velocity and flow rate of the blood flow in the CRA.* The centerline velocity v_z^* and the flow rate Q^* at the outlet section of the CRA ($z = L$) are computed using the mathematical model for different values of intraocular pressures (IOP), and normalized with respect to their value at IOP = 15 mmHg.

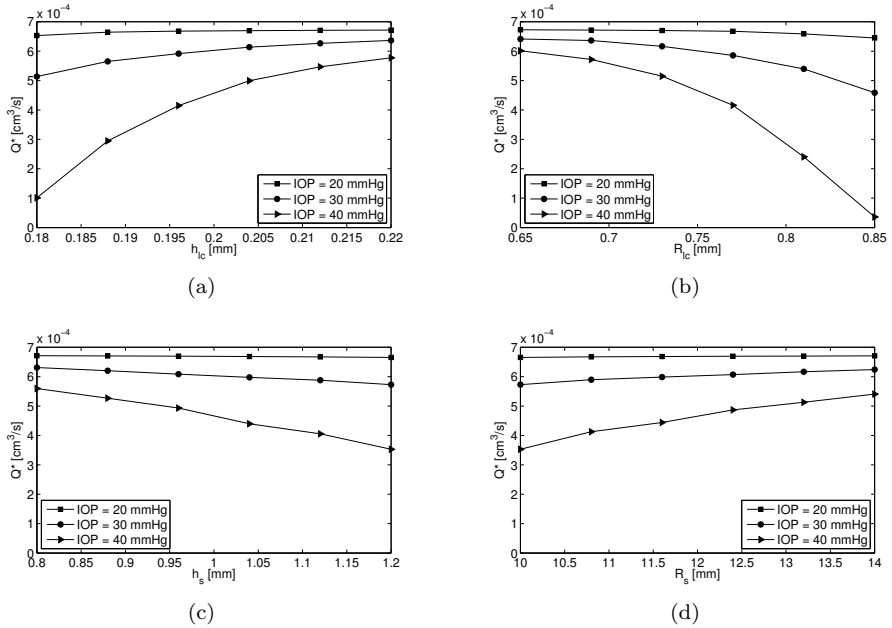

FIGURE 14. *Effect of variations in scleral and laminar geometry on the flow rate Q^* of the central retinal artery (CRA).* Q^* is computed for intraocular pressure equal to 20, 30, and 40 mmHg, as laminar thickness h_{lc} (a), laminar radius R_{lc} (b), scleral thickness h_s (c) and scleral radius R_s (d) are varied.

- the resistance to flow of the central retinal artery increases, inducing a reduction in velocity.

The presence of compressive regions in the lamina cribrosa have been suggested by several authors. Morgan et al. recorded an increases in tissue pressure at the anterior level of the lamina cribrosa as they advanced a micropipette, coupled to a servo null pressure system, in the eyes of anesthetized dogs [42]. While assessing the response of the anterior lamina cribrosa and prelaminar tissue to acute IOP elevation in glaucoma patients and healthy subjects, Aguomi et al. argued that acute optic disc surface changes represent compression of prelaminar tissue rather than laminar displacement [1]. Using computational models to study the different modes of deformation that occur in the optic nerve head as a result of an increase in IOP, Sigal et al. found that there were substantial differences in the magnitudes of the various modes of strain, with the largest strains being in compression, followed by shearing and finally by extension [56, 57]. Nevertheless, the question of whether or not compressive stress arises in vivo in the lamina cribrosa of humans for some IOP levels is still controversial. Stress distributions in the ocular tissues cannot be measured directly, and therefore we have to rely on indirect measurements.

The decrease in the CRA blood velocity induced by IOP elevation measured in vivo in humans by Harris et al. [27] and Findl et al. [13], shown by the data reported in Figures 10 and 11, seems to be one of these indirect measurements. The agreement between model predictions and experimental results for IOP between 15 and 40 mmHg is very satisfactory when the lamina compression is taken into account, while the agreement deteriorates for IOP beyond 25 mmHg if the lamina compression is not taken into account. This interpretation of clinical results using our mathematical model suggests that regions of radial compressive stress in the lamina cribrosa may indeed develop for elevated IOP levels.

Our model also predicts that the clinically-observed decrease in CRA blood velocity induced by IOP elevation is accompanied by a decrease in CRA lumen, leading to a decrease in blood supply to the retina even more pronounced than the decrease in velocity measured with Color Doppler Imaging, as shown in Figures 12 and 13. Also, Figure 14 shows that the extent of this reduction varies among individuals depending on the radius and thickness of their sclera and lamina cribrosa. These findings suggest that the same IOP level might have different consequences on the CRA hemodynamics for different individuals and, in particular, lead to different alterations in the blood supply to the retina.

The model is based on numerous simplifying assumptions. In particular, the lamina cribrosa is assumed to be homogeneous and isotropic, and the central perforation allowing the passage of the CRA is neglected. The outlet pressure in the CRA segment is very likely to be affected by the constriction caused by the compression of the lamina cribrosa on the central retinal vein, and the effect would become more significant as IOP increases. This effect is neglected here and the outlet pressure P_L is kept constant and independent of IOP. Also, the sclera affects the lamina cribrosa via the lateral tension computed by the Laplace's law, but the sclera is not affected by the presence of the lamina. Similarly, the lamina cribrosa affects the CRA via the radial compression acting on a portion of the CRA external wall, but the lamina is not affected by the presence of the CRA. To assess the validity of such assumptions, we have used experimental and clinical studies. The model for the lamina cribrosa has been validated against the data obtained in dogs by Morgan et al. [42, 43]. The model for the coupling between the lamina cribrosa and the CRA

hemodynamics has been validated against two different sets of clinical data, namely those by Harris et al. [27] and those by Findl et al. [13]. The agreement between the model predictions and the experimental/clinical data from these three different and unrelated studies is very satisfactory, as shown in Figures 6, 10 and 11, and this provides a good validation of our model.

Further developments of the modeling approach described in this paper seems to be a promising direction of research. For example, more detailed models of the optic nerve head and sclera could be included in order to perform patient-specific simulations.

6. **Conclusions.** This paper presents a model based on the physical principles of elasto-mechanics and fluid-dynamics to describe the relationship between the action of intraocular pressure, the deformation of the lamina cribrosa and the CRA hemodynamics. Our model suggests that the mechanical factor behind the clinically-observed velocity reduction in the CRA after acute IOP elevation is the compression exerted on the CRA by the lamina cribrosa. The model also predicts that the same IOP elevation would induce different CRA hemodynamic responses in eyes with different anatomical features. The model predictions suggest that individual variations of the lamina's geometric properties may result in significantly different CRA hemodynamic responses to IOP elevation. These different individual responses may help explaining why susceptibilities to a given level of IOP differ among individuals and may help revealing how retinal ischemic damage may occur during IOP elevations in certain individuals.

Acknowledgments. We would like to thank the referees for their valuable comments and suggestions. This work was partially supported by the NSF/DMS grants 1134731 and 1224195, the NIH grant 1R21EY022101-01A1, the Indiana University Collaborative Research Grant fund of the Office of the Vice President for Research and Unrestricted Grant from Research to Prevent Blindness.

REFERENCES

[1] Y. Aguomi, G. P. Sharpe, D. H. Hutchison, M. T.Nicolela, P. H.Artes and B. C. Chauhan, Laminar and pre laminar tissue displacement during intraocular pressure elevation in glaucoma patients and healthy controls, *Ophthalmology*, **118** (2011), 52–59.

[2] R. L. Armentano, J. G. Barra, J. Levenson, A. Simon and R. H. Pichel, Arterial wall mechanics in conscious dogs: Assessment of viscous, inertial, and elastic moduli to characterize aortic wall behavior, *Circ. Res.*, **76** (1995), 468–478.

[3] D. Badeanu, M. Ritt, J. Harazny, J. Heckmann, R. E. Schmieder and G. Michelson, Wall-to-lumen ratio of retinal arterioles and arteriole-to-venule ratio of retinal vessels in patients with cerebrovascular damage, *Invest. Ophthalmol. Vis. Sci.*, **50** (2009), 4351–4359.

[4] R. R Buhrmann, H. A. Quigley, Y. Barron, S. K. West, M. S. Oliva and B. B. O. Mmbaga, Prevalence of glaucoma in a rural East African population, *Invest. Ophthalmol. Vis. Sci.*, **41** (2000), 40–48.

[5] C. F. Burgoyne, J. C. Downs, A. J. Bellezza, J. K. F. Suh and R. T. Hart, The optic nerve head as a biomechanical structure: A new paradigm for understanding the role of IOP-related stress and strain in the pathophysiology of glaucomatous optic nerve head damage, *Prog. Retin. Eye Res.*, **24** (2005), 39–73.

[6] J. Caprioli and A. L. Coleman, Blood pressure, perfusion pressure, and glaucoma, *Am. J. Ophthalmol.*, **149** (2010), 704–712.

[7] V. P. Costa, R. Lauande-Pimentel, R. A. Fonseca and L. Magacho, The influence of age, sex, race, refractive error and optic disc parameters on the sensitivity and specificity of scanning laser polarimetry, *Acta Ophthalmol. Scand.*, **82** (2004), 419–425.

[8] J. E. De León-Ortega, L. M. Sakata, B. E. Monheit, G. Jr McGwin, S. N Arthur and C. A. Girkin, Comparison of diagnostic accuracy of Heidelberg Retina Tomograph II and Heidelberg Retina Tomograph 3 to discriminate glaucomatous and nonglaucomatous eyes, *Am. J. Ophthalmol.*, **144** (2007), 525–532.
[9] H. Dongqi and R. Zeqin, A biomathematical model for pressure-dependent lamina cribrosa behavior, *J. Biomech.*, **32** (1999), 579–584.
[10] G. T. Dorner, E. Polska, G. Garhöfer, C. Zawinka, B. Frank and L. Schmetterer, Calculation of the diameter of the central retinal artery from noninvasive measurements in humans, *Curr. Eye Res.*, **25** (2002), 341–345.
[11] M. E. Edwards and T. A. Good, Use of a mathematical model to estimate stress and strain during elevated pressure induced lamina cribrosa deformation, *Curr. Eye Res.*, **23** (2001), 215–225.
[12] R. Ehrlich, A. Harris, N. S. Kheradiya, D. M. Winston, T. A. Ciulla and B. Wirostko, Age-related macular degeneration and the aging eye, *Clin. Interv. Aging.*, **3** (2008), 473–482.
[13] O. Findl, K. Strenn, M. Wolzt, R. Menapace, C. Vass, H. G. Eichler and L. Schmetterer, Effects of changes in intraocular pressure on human ocular haemodynamics, *Curr. Eye Res.*, **16** (1997), 1024–1029.
[14] J. Flammer, M. Pache and T. Resink, Vasospasm, its role in the pathogenesis of diseases with particular reference to the eye, *Prog. Retin. Eye Res.*, **20** (2001), 319–349.
[15] FreeFem++, version 3.12-0 (2d and 3d), *Université Pierre et Marie Curie Laboratoire Jacques-Louis Lions*, `http://www.freefem.org/ff++/`.
[16] Y. C. Fung, *Biomechanics: Circulatio*, 2^{nd} edition, Springer-Verlag, New York, 1997.
[17] Y. C. Fung, *Biomechanics: Mechanical Properties of Living Tissues*, 2^{nd} edition, Springer-Verlag, New York, 1993.
[18] P. Ganesan, S. He and H. Xu, Development of an image-based network model of retinal vasculature, *Ann. Biomed. Eng.*, **38** (2010), 1566–1585.
[19] P. Ganesan, S. He and H. Xu, Analysis of retinal circulation using an image-based network model of retinal vasculature, *Microvasc. Res.*, **80** (2010), 99–109.
[20] P. Ganesan, S. He and H. Xu, Development of an image-based model for capillary vasculature of retina, *Comput. Methods Programs Biomed.*, **102** (2011), 35–46.
[21] P. Ganesan, S. He and H. Xu, Modelling of pulsatile blood flow in arterial trees of retinal vasculature, *Med. Eng. Phys.*, **33** (2011), 810–823.
[22] C. A. Girkin, G. Jr McGwin, S. F. McNeal and J. DeLeon-Ortega, Racial differences in the association between optic disc topography and early glaucoma, *Invest. Ophthalmol. Vis. Sci.*, **44** (2003), 3382–3387.
[23] C. A. Girkin, G. Jr McGwin, C. Long, J. DeLeon-Ortega, C. M. Graf and A. W. Everett, Subjective and objective optic nerve assessment in African Americans and whites, *Invest. Ophthalmol. Vis. Sci.*, **45** (2004), 2272–2278.
[24] C. A. Girkin, G. Jr McGwin, A. Xie and J. E. Deleon-Ortega, Differences in optic disc topography between black and white normal subjects, *Ophthalmology*, **112** (2005), 33–39.
[25] C. A. Girkin, P. A. Sample, J. M. Liebmann, S. Jain, C. Bowd, L. M. Becerra, F. A. Medeiros, L. Racette, K. A. Dirkes and R. N. Weinreb, African Descent and Glaucoma Evaluation Study (ADAGES): II. Ancestry differences in optic disc, retinal nerve fiber layer, and macular structure in healthy subjects, *Arch. Ophthalmol.*, **128** (2010), 541–550.
[26] G. Guidoboni, A. Harris, J.C. Arciero, B.A. Siesky, A. Amireskandari, A.L. Gerber, A.H. Huck, N.J. Kim, S. Cassani and L. Carichino, *Mathematical modeling approaches in the study of glaucoma disparities among people of African and European Descents*, J. Coupled Syst. Multiscale Dyn., **1**(1) (2013), 1-21.
[27] A. Harris, K. Joos, M. Kay, D. Evans, R. Shetty, W. E. Sponsel and B. Martin, Acute IOP elevation with scleral suction: Effects on retrobulbar haemodynamics, *Br. J. Ophthalmol.*, **80** (1996), 1055–1059.
[28] A. Harris, C. P. Jonescu-Cuypers, L. Kagemann, T. A. Ciulla and G. K. Krieglstein, *Atlas of Ocular Blood Flow. Vascular Anatomy, Pathophysiology, and Metabolism*, Elsevier, Philadelphia, 2003.
[29] A. Harris, L. Kagemann, R. Ehrlich, C. Rospigliosi, D. Moore and B. Siesky, Measuring and interpreting ocular blood flow and metabolism in glaucoma, *Can. J. Ophthalmol.*, **43** (2008), 328–336.

[30] A. Harris, G. Guidoboni, J.C. Arciero, A. Ameriskandari, L.A. Tobe and B.A. Siesky, *Ocular hemodynamics and glaucoma: the role of mathematical modeling*, Eur. J. Ophthalmol., **23**(2) (2013), 139-146.
[31] S. S. Hayreh, Blood flow in the optic nerve head and factors that may influence it, *Prog. Retin. Eye Res.*, **20** (2001), 595–624.
[32] E. M. Hoffmann, L. M. Zangwill, J. G. Crowston and R. N. Weinreb, Optic disk size and glaucoma, *Surv. Ophthalmol.*, **52** (2007), 32–49.
[33] I. Januleviciene, R. Ehrlich, B. Siesky, I. Nedzelskiene and A. Harris, Visual function, optic nerve structure, and ocular blood flow parameters after 1 year of glaucoma treatment with fixed combinations, *Eur. J. Ophthalmol.*, **19** (2009), 790–797.
[34] J. B. Jonas, C. Y. Mardin, U. Schlötzer-Schrehardt and G. O. Naumann, Morphometry of the human lamina cribrosa surface, *Invest. Ophthalmol. Vis. Sci.*, **32** (1991), 401–405.
[35] J. B. Jonas and L. Holbach, Central corneal thickness and thickness of the lamina cribrosa in human eyes, *Invest. Ophthalmol. Vis. Sci.*, **46** (2005), 1275–1279.
[36] O. Knight, C. A. Girkin, D. L. Budenz, M. K. Durbin and W. J Feuer, Effect of race, age, and axial length on optic nerve head parameters and retinal nerve fiber layer thickness measured by Cirrus HD-OCT, *Arc. Ophthalmol.*, **130** (2012), 312–318.
[37] M. C. Leske, A. M. S. Connell, A. P. Schachat and L. Hyman, The Barbados Eye Study: Prevalence of open angle glaucoma, *Arc. Ophthalmol.*, **112** (1994), 821–829.
[38] M. C. Leske, Open-angle glaucoma – an epidemiologic overview, *Ophthalmic Epidemiol.*, **14** (2007), 166–172.
[39] M. C. Leske, A. Heijl, L. Hyman, B. Bengtsson, L. Dong and Z. Yang, Predictors of long-term progression in the early manifest glaucoma trial, *Ophthalmology*, **114** (2007), 1965–1972.
[40] A. Mikelic, G. Guidoboni and S. Canic, Fluid-structure interaction in a pre-stressed tube with thick elastic walls I: the stationary Stokes problem, *Netw. Heterog. Media*, **2** (2007), 397–423.
[41] D. Moore, A. Harris, D. Wudunn, N. Kheradiya and B. Siesky, Dysfunctional regulation of ocular blood flow: a risk factor for glaucoma?, *Clin. Ophthalmol.*, **2** (2008), 849–861.
[42] W. H Morgan, D. Y. Yu, V. A. Alder, S. J. Cringle, R. L. Cooper, P. H. House and I. J. Constable, The correlation between cerebrospinal fluid pressure and retrolaminar tissue pressure, *Invest. Ophthalmol. Vis. Sci.*, **39** (1998), 3236–3242.
[43] W. H Morgan, B. C. Chauhan, D. Y. Yu, S. J. Cringle, V. A. Alder and P. H. House, Optic disc movement with variations in intraocular and cerebrospinal fluid pressure, *Invest. Ophthalmol. Vis. Sci.*, **43** (2002), 1419–1428.
[44] J. Morgan-Davies, N. Taylor, A. R. Hill, P. Aspinall, C. J. O'Brien and A. Azuara-Blanco, Three dimensional analysis of the lamina cribrosa in glaucoma, *Br. J. Ophthalmol.*, **88** (2004), 1299–1304.
[45] T. Newson and A. El-Sheikh, Mathematical modeling of the biomechanics of the lamina cribrosa under elevated intraocular pressures, *J. Biomech. Eng.*, **128** (2006), 496–504.
[46] R. E. Norman, J. G. Flanagan, S. M. K. Rausch, I. A. Sigal, I. Tertinegg, A. Eilaghi, S. Portnoy, J. G. Sled and C. R. Ethier, Dimensions of the human sclera: Thickness measurement and regional changes with axial length, *Exp. Eye Res.*, **90** (2010), 277–284.
[47] B. Pemp and L. Schmetterer, Ocular blood flow in diabetes and age-related macular degeneration, *Can. J. Ophthalmol.*, **43** (2008), 295–301.
[48] D. Poinoosawmy, L. Fontana, J. X. Wu, F. W. Fitzke and R. A. Hitchings, Variation of nerve fibre layer thickness measurements with age and ethnicity by scanning laser polarimetry, *Br. J. Ophthalmol.*, **81** (1997), 350–354.
[49] C. J. Pournaras, E. Rungger-Brändle, C. E. Riva, S. H. Hardarson and E. Stefansson, Regulation of retinal blood flow in health and disease, *Prog. Retin. Eye Res.*, **27** (2008), 284–330.
[50] A. Quarteroni, M. Tuveri and A. Veneziani, Computational vascular fluid dynamics: Problems, models and methods, *Comput. Visual Sci.*, **2** (2000), 163–197.
[51] L. Racette, M. R. Wilson, L. M. Zangwill, R. N. Weinreb and P. A. Sample, Primary open-angle glaucoma in blacks: A review, *Surv. Ophthalmol.*, **48** (2003), 295–313.
[52] L. Racette, C. Boden, S. L. Kleinhandler, C. A. Girkin, J. M. Liebmann, L. M. Zangwill, F. A. Medeiros, C. Bowd, R. N. Weinreb and M. R. Wilson, Differences in visual function and optic nerve structure between healthy eyes of blacks and whites, *Arch. Ophthalmol.*, **123** (2005), 1547–1553.
[53] R. Ren, N. Wang, B. Li, L. Li, F. Gao, X. Xu and J. B. Jonas, Lamina cribrosa and peripapillary sclera histomorphometry in normal and advanced glaucomatous Chinese eyes with various axial length, *Invest. Ophthalmol. Vis. Sci.*, **50** (2009), 2175–2184.

[54] M. I. Seider, R. Y. Lee, D. Wang, M. Pekmezci, T. C. Porco and S. C. Lin, Optic disk size variability between African, Asian, white, Hispanic, and Filipino Americans using Heidelberg retinal tomography, *J. Glaucoma*, **18** (2009), 595–600.
[55] I. A. Sigal, J. G. Flanagan, I. Tertinegg and C. R. Ethier, Finite element modeling of optic nerve head biomechanics, *Invest. Ophthalmol. Vis. Sci.*, **45** (2004), 4378–4387.
[56] I. A. Sigal, J. G. Flanagan, I. Tertinegg and C. R. Ethier, Predicted extension, compression and shearing of optic nerve head tissues, *Exp. Eye Res.*, **85** (2007), 312–322.
[57] I. A. Sigal, J. G. Flanagan, I. Tertinegg and C. R. Ethier, Modeling individual-specific human optic nerve head biomechanics. Part I: IOP-induced deformations and influence of geometry, *Biomech. Model. Mechanobiol.*, **8** (2009), 85–98.
[58] I. A. Sigal, H. Yang, M. D. Roberts, J. L. Grimm, C. F. Burgoyne, S. Demirel and J. C. Downs, IOP-induced lamina cribrosa deformation and scleral canal expansion: Independent or related?, *Invest. Ophthalmol. Vis. Sci.*, **52** (2011), 9023–9032.
[59] I. A. Sigal, R. A. Bilonick, L. Kagemann, G. Wollstein, H. Ishikawa, J. S. Schuman and J. L. Grimm, The optic nerve head as a robust biomechanical system, *Invest. Ophthalmol. Vis. Sci.*, **53** (2012), 2658–2667.
[60] I. A. Sigal and J. L. Grimm, A few good responses: which mechanical effects of IOP on the ONH to study?, Invest. Ophthalmol. Vis. Sci., **53**(7) (2012), 4270–4278.
[61] I. A. Sigal, J. G. Flanagan, K. L. Lathrop, I. Tertinegg and R. Bilonick, Human lamina cribrosa insertion and age, *Invest. Ophthalmol. Vis. Sci.*, **53** (2012), 6870–6879.
[62] A. Sommer, J. M. Tielsch, J. Katz, H. A. Quigley, J. D. Gottsch, J. C. Javitt, J. F. Martone, R. M. Royall, K. A. Witt and S. Ezrine, Racial differences in the cause-specific prevalence of blindness in east Baltimore, *N. Engl. J. Med.*, **325** (1991), 1412–1417.
[63] A. Sommer, Glaucoma risk factors observed in the Baltimore Eye Survey, *Curr. Opin. Ophthalmol.*, **7** (1996), 93–98.
[64] T. Takahashi, T. Nagaoka, H. Yanagida, T. Saitoh, A. Kamiya, T. Hein, L. Kuo and A. Yoshida, A mathematical model for the distribution of hemodynamic parameters in the human retinal microvascular network, *J. Biorheol.*, **23** (2009), 77–86.
[65] J. M. Tielsch, A. Sommer, J. Katz, R. M. Royall, H. A. Quigley and J. Javitt, Racial variations in the prevalence of primary open-angle glaucoma: The Baltimore Eye Survey, *JAMA*, **266** (1991), 369–374.
[66] R. Varma, J. M. Tielsch, H. A. Quigley, S. C. Hilton, J. Katz, G. L. Spaeth and A. Sommer, Race-, age-, gender-, and refractive error-related differences in the normal optic disc, *Arch. Ophthalmol.*, **112** (1994), 1068–1076.
[67] S. Woo, A. S. Kobayashi, W. A. Schlegel and C. Lawrence, Nonlinear material properties of intact cornea and sclera, *Exp. Eye Res.*, **14** (1972), 29–39.
[68] J. R. Zelefsky, N. Harizman, R. Mora, E. Ilitchev, C. Tello, R. Ritch and J. M. Liebmann, Assessment of a race-specific normative HRT-III database to differentiate glaucomatous from normal eyes, *J. Glaucoma*, **15** (2006), 548–551.

Received May 21, 2012; Accepted August 30, 2013.

E-mail address: gguidobo@math.iupui.edu
E-mail address: alharris@indiana.edu
E-mail address: lcarichi@iupui.edu
E-mail address: arieli@jct.ac.il
E-mail address: bsiesky@indiana.edu